Geophysical Research Letters

RESEARCH LETTER
10.1029/2021GL092440

Key Points:

- Intermediate currents in the southwest tropical Pacific show a significant interannual response to ENSO at a 7–12-month lag
- Intermediate seasonal and interannual variations are induced by Rossby waves from different baroclinic modes and different originations
- Southwestern tropical Pacific coastline enhances intermediate seasonal explained variance and relationship between currents and ENSO

Supporting Information:

- Supporting Information S1

Correspondence to:
F. Wang,
fwang@qdio.ac.cn

Citation:
Wang, J., Ma, Q., Wang, F., & Zhang, D. (2021). Linking seasonal-to-interannual variability of intermediate currents in the southwest tropical Pacific to wind forcing and ENSO. *Geophysical Research Letters*, *48*, e2021GL092440. https://doi.org/10.1029/2021GL092440

Received 7 JAN 2021
Accepted 22 JAN 2021

Linking Seasonal-to-Interannual Variability of Intermediate Currents in the Southwest Tropical Pacific to Wind Forcing and ENSO

Jianing Wang[1,2,3], Qiang Ma[1,2], Fan Wang[1,2,3], and Dongxiao Zhang[4,5]

[1]Key Laboratory of Ocean Circulation and Waves, Institute of Oceanology, Center for Ocean Mega-Science, Chinese Academy of Sciences, Qingdao, China, [2]Function Laboratory for Ocean Dynamics and Climate, Pilot National Laboratory for Marine Science and Technology Qingdao, Qingdao, China, [3]University of Chinese Academy of Sciences, Beijing, China, [4]Cooperative Institute for Climate, Ocean and Ecosystem Studies, University of Washington, Seattle, WA, USA, [5]Pacific Marine and Environmental Laboratory, NOAA, Seattle, WA, USA

Abstract Seasonal-to-interannual variability of intermediate circulations in the southwest tropical Pacific is key to interhemisphere and interbasin water mass exchange and is shown to be interconnected with wind forcing and the El Niño–Southern Oscillation (ENSO) based on numerical model results validated by mooring observations. The Lower Equatorial Intermediate Current and the intermediate part of the New Guinea Coastal Undercurrent show clear seasonal variability and a significant interannual response to ENSO at a 7–12-month lag, both of which are induced by Rossby waves. Baroclinic modes 1 and 2 of the direct wind-forced Rossby waves contribute mainly to the seasonal variability. In contrast, the Rossby waves from baroclinic modes 2 and 4 and the reflection of Kelvin waves are the main contributors to the variability on ENSO time scales. The presence of the southwest tropical Pacific coastline enhances the intermediate seasonal variance and the interannual relationship between intermediate currents and ENSO.

Plain Language Summary The variability of intermediate circulations at seasonal-to-interannual time scales is essential to water mass redistribution and is demonstrated to be closely linked to wind forcing and the El Niño–Southern Oscillation (ENSO) based on reanalysis product and linear continuously stratified model experiments validated by mooring observations. The Lower Equatorial Intermediate Current (LEIC) and the New Guinea Coastal Undercurrent (NGCUC-I) at intermediate depths of 400–1,000 m exhibit evident seasonal variability, which is induced by the first two baroclinic Rossby waves. Intermediate zonal velocity anomalies at the LEIC, NGCUC-I, and two 5°N/5°S zonal bands are highly correlated with the Niño-3.4 index at a 7–12-month lag, which is attributed to baroclinic modes 2 and 4 Rossby waves. The intermediate seasonal variability is caused by direct wind-forced Rossby waves. In contrast, Rossby waves from the reflection of Kelvin waves play a critical role in the interannual variability. The presence of Papua New Guinea coastline enhances the seasonal variance of the LEIC and increases the peak value of the lead-lag correlation between the LEIC and ENSO.

1. Introduction

The intermediate circulations in the southwest tropical Pacific (SWTP) contribute to the interhemispheric and interbasin exchanges of water masses and biogeochemical properties. Significant progress has been made in the past decades in understanding the surface and subsurface circulations at depths shallower than 400 m (e.g., Gouriou & Toole, 1993; F. Wang et al., 2016). A recent review by Ménesguen et al. (2019) summarized previously observed main features (e.g., Cravatte et al., 2012; Eriksen, 1981; Firing, 1987; Johnson et al., 2002) and the formation mechanisms of intermediate and deep equatorial circulations (e.g., Ascani et al., 2010, 2015; d'Orgeville et al., 2007; Hua et al., 2008; Qiu et al., 2013). However, observations of middepth circulations below 400 m are still sparse, and there remain large gaps in our understanding of their structure and variability. In this paper, we seek to describe and analyze the intermediate seasonal-to-interannual variability in the SWTP.

The circulations within the 400–1,000 m depth range in the SWTP (Figure S1a) can be briefly described as follows. On the equator, the Equatorial Intermediate Current (EIC) and the Lower Equatorial

Intermediate Current (LEIC) lie beneath the Equatorial Undercurrent (EUC) between ~1°S and 1°N (Firing et al., 1998; Gouriou et al., 2006; Johnson et al., 2002; Marin et al., 2010). The annual mean EIC and LEIC flow westward but reverse seasonally to eastward currents. In the region close to the Papua New Guinea (PNG) coastline, the intermediate part of the northwestward-flowing New Guinea Coastal Undercurrent exists (referred to as NGCUC-I hereinafter; Kawabe et al., 2008; Zenk et al., 2005).

The seasonal variability in the LEIC (denoting both EIC and LEIC for convenience hereafter) velocity and temperature is induced by the vertical propagation of the first meridional Rossby wave, which is directly forced by the westward-propagating seasonal zonal wind fields (Kessler & McCreary, 1993; Marin et al., 2010). Our companion paper (Ma et al., 2020) found that the interannual anomaly of LEIC velocity at 142°E is mainly related to the second baroclinic mode of Rossby waves triggered by wind anomalies during the El Niño–Southern Oscillation (ENSO) mature stage. When the variability anomalies at seasonal, interannual, and intraseasonal time scales were larger than the mean currents on which they superimposed, the disappearance of the LEIC was observed at different longitudes (Cravatte et al., 2017; Firing et al., 1998; Ma et al., 2020; Marin et al., 2010). The seasonal variation of NGCUC-I is inversely correlated with that of the LEIC (Kawabe et al., 2008; Zenk et al., 2005). Kawabe et al. (2008) observed the interannual changes in the LEIC and NGCUC-I before and after the 1998–1999 La Niña event. The dynamics and interconnected relationships between seasonal and interannual variability are even less known, especially in the SWTP where the PNG coastline could exert a potential influence.

Our goal, therefore, is to provide a more complete description and dynamic understanding of the seasonal-to-interannual variability of the intermediate currents in the SWTP, through long-term mooring measurements and numerical models. Mooring observations made recently and in the 1990s are first used to validate the performance of an ocean reanalysis product and linear continuously stratified (LCS) ocean model experiments. Then, the ocean reanalysis product is analyzed, and additional LCS experiments are designed to achieve our goal.

2. Data

2.1. Mooring Data

As a part of the Scientific Observing Network of the Chinese Academy of Sciences, three subsurface moorings were deployed in the region north of PNG. Their longitudes/latitudes are 142°E/0°, 142°E/1°S, and 141.4°E/1.7°S (Figure S1a). The measurement period of mooring at 142°E/0° was from August 2014 to December 2018, and those of the other two were from November 2015 to December 2018. One upward-looking and one downward-looking Teledyne RD Instruments 75 kHz acoustic Doppler current profilers (ADCPs) were mounted on the main float at ~500 m. The two ADCPs returned the hourly velocity profiles over the depth range of 50–950 m with a vertical bin size of 8 m and a frequency of 35 pings. The data were then interpolated vertically to 1-m intervals.

As a part of the Tropical Ocean Climate Study (TOCS) project of Japan Agency for Marine-Earth Science and Technology, hourly layered velocity from September 1998 to October 2002 was observed by moored current meters at mean nominal depth of 735 m (an average of 700, 733, and 773 m) at 142°E/2.5°S and 787 m at 138°E/0° (Figure S1a; Kawabe et al., 2008; Ueki et al., 2003).

2.2. Reanalysis Product GLORYS12V1

To help resolve the large spatiotemporal scales of the intermediate circulations, we also use the daily and monthly velocity data over 1993–2018 from the global ocean physical reanalysis product GLORYS12V1 (hereinafter GL12) provided by the Copernicus Marine Environment Monitoring Service. The model platform of GL12 is based on the Nucleus for European Modeling of the Ocean (NEMO) with a horizontal resolution of 1°/12° in longitude/latitude and 50 vertical levels. Altimeter data, in situ temperature and salinity vertical profiles, and satellite sea surface temperature are jointly assimilated (Lellouche et al., 2018).

2.3. LCS Model

To reveal the underlying mechanisms of intermediate seasonal-to-interannual variability, we performed numerical experiments with the LCS model (McCreary, 1981; Shankar et al., 1996; Yu & McPhaden, 1999). The LCS model is configured to the Pacific Ocean between 20°S–20°N and 100°E–70°W with horizontal resolutions of 0.25° × 0.25°. The modeled velocity profile is interpolated from 0 to 4,000 m with a 10-m vertical resolution. The total solution here is the sum of the first 10 baroclinic modes. The model is spun up for 10 years forced by monthly mean climatology of Cross-Calibrated Multi-Platform version 2.0 (CCMP v2.0) satellite winds during 1993–2018 (Atlas et al., 2011). The climatology run is used as the restart state for all experiments. The main run (referred to as LCS-MR) integrates forward in time for the period of 1993–2018 using monthly CCMP winds. See supporting information Text S1 for more details about the LCS model.

The westward-propagating Rossby waves arise from the direct forcing of easterly winds and the reflection of equatorial Kelvin waves in the eastern tropical Pacific. To evaluate their relative importance, we conduct the LCS experiment using a damper within 15°S–15°N and 85°W–80°W in the eastern Pacific (LCS-Damp). In LCS-Damp, the damper can efficiently absorb the energy of the incoming equatorial Kelvin waves, while the other settings are the same as LCS-MR. Therefore, LCS-Damp represents the sole contribution from direct wind forcing, and the difference between LCS-MR and LCS-Damp (LCS-Reflect) can measure the contribution from the reflected Kelvin-to-Rossby waves.

A previous study (Zhang et al., 2020) suggests that the tilted PNG coastline can alter the meridional distribution of intermediate intraseasonal variability intensity by influencing the propagation of short Rossby waves. To further estimate the influence of the PNG coastline on the intermediate seasonal-to-interannual variability, we perform the LCS-Topo experiment, in which the islands of Irian Jaya and PNG and those surrounding the Solomon Sea are removed (red frame in Figure S2), while the other settings are the same as LCS-MR.

3. Results

The GL12 and LCS-MR outputs perform well in simulating the seasonal and interannual variability of intermediate circulations in the SWTP. Figure 1 shows the daily time series of the observed and GL12-modeled and LCS-MR-modeled intermediate zonal velocities. The observed and modeled daily time series were smoothed by applying a 61-day running mean to focus on the variations longer than intraseasonal time scales. For both the daily time series before and after deseasonalization, the correlation coefficients of observations with GL12 and LCS-MR at all five mooring locations exceed the 95% confidence level (Table S1). The weak correlation at 142°E/2.5°S may be due to the limited length of the time series. The normalized root-mean-square errors (*NRMSE*) of GL12 and LCS-MR relative to the observations are all less than 35%: $NRMSE = \frac{\sqrt{\frac{1}{n}\sum_1^n \left(U_{\text{observation}} - U_{\text{model}}\right)^2}}{\max\left(U_{\text{observation}}\right) - \min\left(U_{\text{observation}}\right)}$, where n is the number of data values and $\max(U_{\text{observation}})$ and $\min(U_{\text{observation}})$ are the maximum and minimum of the observed zonal velocities, respectively (Table S1). However, the observation periods of all five moorings are too short (3–4 years) to reliably validate the performance of the GL12 and LCS-MR variability on interannual time scales. To remedy this source of uncertainty, we performed an intercomparison between the GL12 and LCS-MR transports over 1993–2018. The LEIC and NGCUC-I transports are calculated by integrating all velocities between 400 and 1,000 m over 0.5°S–0.5°N and 2.0°S–the PNG coastline, respectively. The correlations between GL12 and LCS-MR for both the original (Figures 2a and 2c) and deseasonalized (Figures 2b and 2d) monthly time series are larger than 0.71 for LEIC transport and 0.52 for NGCUC-I transport, and *NRMSE*s are less than 14% for LEIC and 23% for NGCUC-I (Table S2). There is a nearly constant difference of 20 cm s^{-1} between LCS-MR and the observation for the pointwise zonal velocity at 142°E/2.5°S and of 8.5 Sv between LCS-MR and GL12 NGCUC-I transports, respectively. This suggests that the LCS model physics cannot reproduce the mean velocity of western boundary currents very well due to the lack of nonlinear processes. We thus use LCS-MR minus 20 cm s^{-1} at 142°E/2.5°S and LCS-MR minus 8.5 Sv for the NGCUC-I transport in the above evaluation. The nearly constant difference does not influence the interpretation of LCS-MR outputs in the study of seasonal-to-interannual variability.

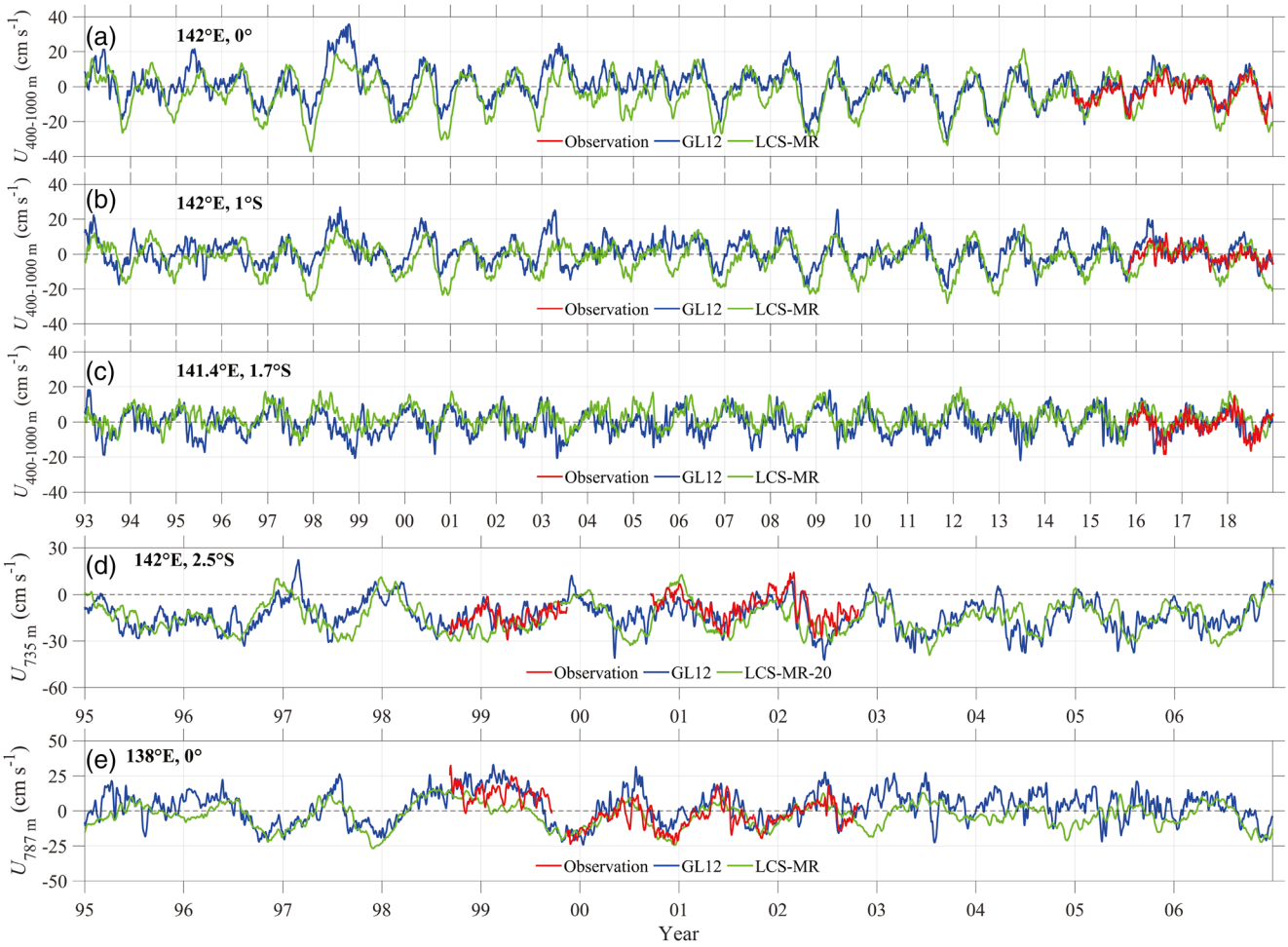

Figure 1. Comparison of daily time series of U averaged over 400–1,000 m at (a) 142°E/0°, (b) 142°E/1°S, and (c) 141.4°E/1.7°S, U at (d) 735 m of 142°E/2.5°S, and U at 787 m of (e) 138°E/0° obtained from mooring observation (red), GL12 (blue), and LCS-MR (green). At 142°E/2.5°S, we use LCS-MR minus 20 cm s^{-1} in the comparison of U.

3.1. Seasonal Variability

To investigate the characteristics and mechanism of the seasonal cycle, we conduct an annual harmonic fit on the GL12 and LCS-MR original monthly intermediate *U* (averaged over 400–1,000 m, same hereinafter) over 1993–2018. For each output from GL12 or LCS-MR, we calculate the percentage of explained variance for the annual harmonic in the original zonal velocities: R^2 = variance(annual harmonic fit)/variance(original). The phase for the annual harmonic fit is defined as the month of the strongest westward currents. Two regions with large explained variance of $R^2 > 40\%$ can be identified in GL12 (Figure 3a): the LEIC region over 135°E–180° along the equator and the NGCUC-I region over 135°E–145°E along the PNG coastline. The horizontal distributions of LCS-MR R^2 and phase (Figures 3c and 3d) greatly resemble those of GL12 (Figures 3a and 3b), especially for the above two regions. At 142°E, the annual harmonics of the GL12 and LCS-MR transports explain 42% and 56% of the total variance for the LEIC, and 59% and 57% for the NGCUC-I, respectively (Figures 2a and 2c). The above analyses suggest that the seasonal variability of intermediate currents is evident, and LCS-MR can be used to gain insight into their underlying mechanism.

Given that the winds are the only external forcing for LCS-MR and the phase shifts later from east to west, the seasonal cycle is related to the wind-driven annual Rossby waves. The phase shifts later by approximately 4–5 months from 3°S to the equator and then shifts earlier to 3°N, implying the dominance of the first meridional Rossby wave (Figure 3d; Ishizaki et al., 2014). For the baroclinic modes, the phase distribution of the sum of modes 1 and 2 can nearly represent that of the total 10 modes, but any mode 1 or 2 only fails

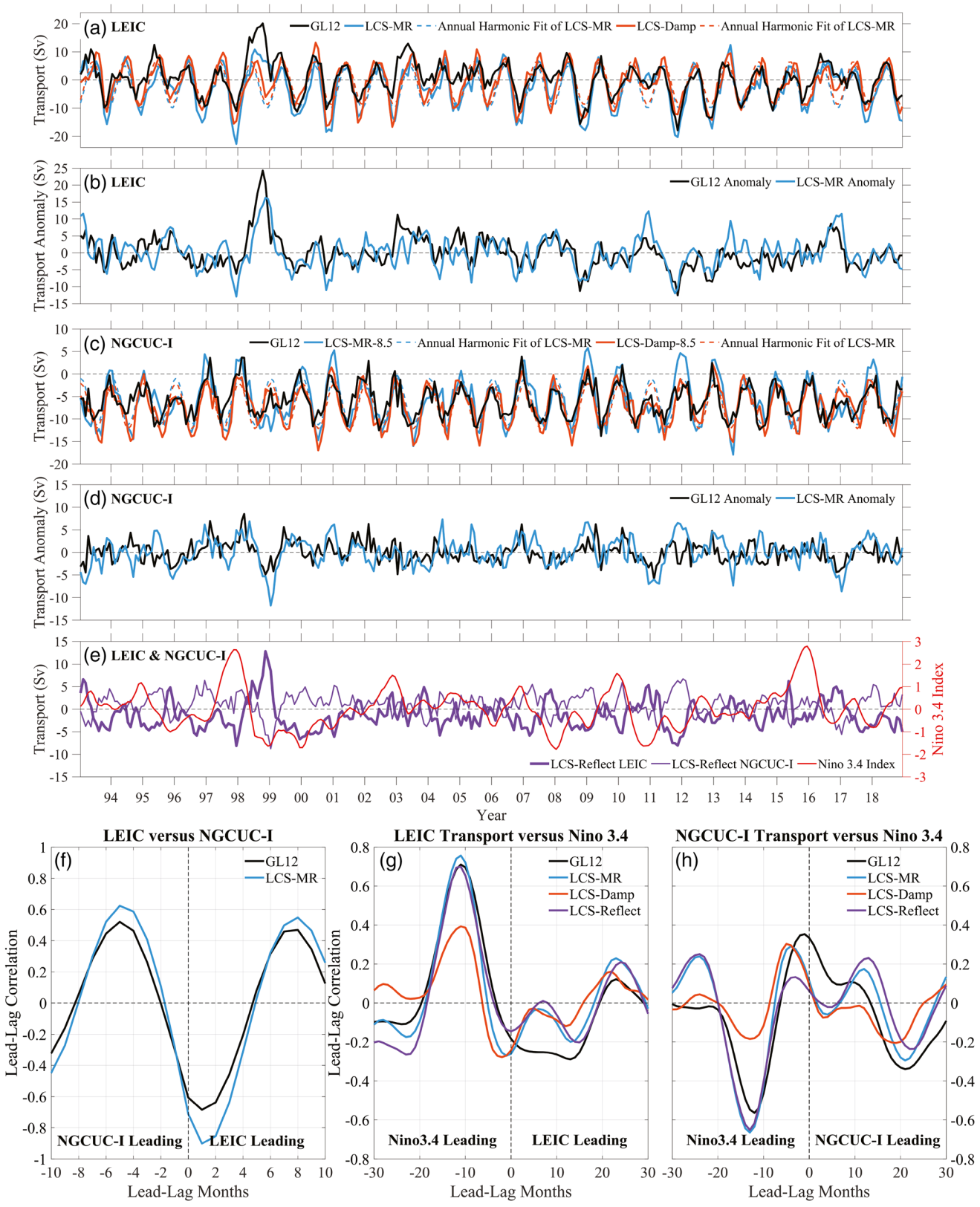
(a) LEIC
GL12
LCS-MR
Annual Harmonic Fit of LCS-MR
LCS-Damp
Annual Harmonic Fit of LCS-MR
Transport (Sv)
(b) LEIC
GL12 Anomaly
LCS-MR Anomaly
Transport Anomaly (Sv)
(c) NGCUC-I
GL12
LCS-MR-8.5
Annual Harmonic Fit of LCS-MR
LCS-Damp-8.5
Annual Harmonic Fit of LCS-MR
Transport (Sv)
(d) NGCUC-I
GL12 Anomaly
LCS-MR Anomaly
Transport Anomaly (Sv)
(e) LEIC & NGCUC-I
Transport (Sv)
Nino 3.4 Index
LCS-Reflect LEIC
LCS-Reflect NGCUC-I
Nino 3.4 Index
94 95 96 97 98 99 00 01 02 03 04 05 06 07 08 09 10 11 12 13 14 15 16 17 18
Year
LEIC versus NGCUC-I
(f)
GL12
LCS-MR
Lead-Lag Correlation
NGCUC-I Leading
LEIC Leading
Lead-Lag Months
LEIC Transport versus Nino 3.4
(g)
GL12
LCS-MR
LCS-Damp
LCS-Reflect
Lead-Lag Correlation
Nino3.4 Leading
LEIC Leading
Lead-Lag Months
NGCUC-I Transport versus Nino 3.4
(h)
GL12
LCS-MR
LCS-Damp
LCS-Reflect
Nino3.4 Leading
NGCUC-I Leading
Lead-Lag Months

to represent most of the features in the total solution (Figures 3k and 3l). To further investigate the contribution of different modes, we calculate the R^2 of cumulative baroclinic modes. Along 142°E, LCS-MR R^2 in the above two regions is largest when only mode 1 is present, decreases to 50%–60% when mode 2 is added, and reaches a stable value of ∼55% when higher baroclinic modes are integrated (Figure S3a). The above analyses suggest that seasonal variability can be mainly attributed to the first meridional and the sum of the first two baroclinic Rossby waves.

In comparison with LCS-MR, LCS-Damp R^2 in the above two regions is larger by 30% (Figure 3e vs. Figure 3c), and the distributions of the seasonal phases (Figure 3f vs. Figure 3d) and amplitudes (figure not shown) are nearly the same. The explained variance from LCS-Reflect (Figures 3g and S3c) almost equals zero, and the phase (Figure 3h) shifts later by 2–6 months compared to LCS-MR. For the LEIC and NGCUC-I transports at 142°E, the time series of annual harmonic fits of LCS-MR and LCS-Damp outputs almost overlap (dashed lines in Figures 2a and 2c), also suggesting nearly the same seasonal phase and amplitude. However, from LCS-Damp to LCS-MR, the explained variance decreases from 71% to 56% for LEIC transport and from 73% to 57% for NGCUC-I transport. This is due to the enhanced overall variance in LCS-MR when the reflected Kelvin-to-Rossby wave is added. Therefore, the annual cycle of intermediate currents is induced by direct wind-driven Rossby waves. The Rossby wave from the reflection of the Kelvin wave increases the overall variance of intermediate currents but has little impact on their seasonal phase and amplitude. As will be shown later in Section 3.2, the reflected Kelvin-to-Rossby wave has profound influence on the intermediate currents on ENSO time scales. LCS-Damp R^2 of baroclinic mode 1 is almost the same as that from LCS-MR (Figure S3b vs. Figure S3a). However, LCS-Damp R^2 becomes higher than that from LCS-MR when the second baroclinic mode is added. When the third and higher modes are further added, the change in LCS-Damp R^2 keeps pace with that of LCS-MR. This suggests that the reflected Kelvin-to-Rossby wave influences the intermediate current variability mainly through the second baroclinic mode.

The PNG coastline contributes to the intermediate seasonal variability in the SWTP. Compared to LCS-MR, LCS-Topo R^2 in the LEIC region west of 145°E and in the NGCUC-I region weakens (Figure 3i vs. Figure 3c). The phase difference between the LEIC and NGCUC-I regions increases from 2 (December vs. October) in LCS-Topo to 4 (December vs. August) months in LCS-MR (Figure 3j vs. Figure 3d).

Furthermore, the LEIC and NGCUC-I transports are interconnected. The lead-lag correlation between the GL12 LEIC and NGCUC-I monthly transports shows two peaks: one with a negative correlation of ∼–0.7 when the LEIC leads NGCUC-I by 1 month and the other with a positive correlation of ∼0.6 when the LEIC lags behind NGCUC-I by 5 months (Figure 2f). LCS-MR shows a similar result but with intensified correlations. These two peaks are associated with the meridional distribution of the annual phase related to the first meridional mode of Rossby wave (Figures 3b and 3d). The negative correlation implies that the westward NGCUC-I could feed the eastward reversing flow of the LEIC, similar to the situation at the subsurface layer where the upper part of the NGCUC feeds the EUC (Kuroda, 2000; Q. Wang et al., 2019).

3.2. Interannual Variability

The intermediate circulations in the SWTP are found to be influenced by the ENSO cycle at the interannual time scale. The lead-lag correlations of the GL12 LEIC and NGCUC-I transport anomalies at 142°E with the Niño-3.4 index show peak values (r_{max}) of ∼0.7 and −0.6 when the Niño-3.4 index leads by ∼10 and ∼11 months, respectively (Figures 2g and 2h). The significant transport anomalies of LEIC and NGCUC-I occur during the following October–November–December months of the 2-year El Niño or La Niña events (Figures 2b and 2d). For the El Niño events, a mean westward transport anomaly of NGCUC-I feeds an eastward transport anomaly of LEIC in a clockwise connected circulation. Their anomalies are reversed to

Figure 2. Time series of LEIC (a) transports from GL12 (black), LCS-MR (blue), and LCS-Damp (orange) and (b) transport anomalies from GL12 (black) and LCS-MR (blue). (c, d) Same as panels (a) and (b), but for NGCUC-I. In (c), we use LCS-MR minus 8.5 Sv in the comparison of NGCUC-I transports. (e) Time series of LEIC and NGCUC-I transports from LCS-Reflect (bold and thin purple curves) and the Niño-3.4 index (red). The lead-lag correlations of (f) NGCUC-I with LEIC transport and of the Niño-3.4 index with (g) LEIC and (h) NGCUC-I transport anomalies obtained from GL12 (black), LCS-MR (blue), LCS-Damp (orange), and LCS-Reflect (purple). LEIC, Lower Equatorial Intermediate Current; LCS, linear continuously stratified ocean model; NGCUC-I, Intermediate part of New Guinea Coastal Undercurrent.

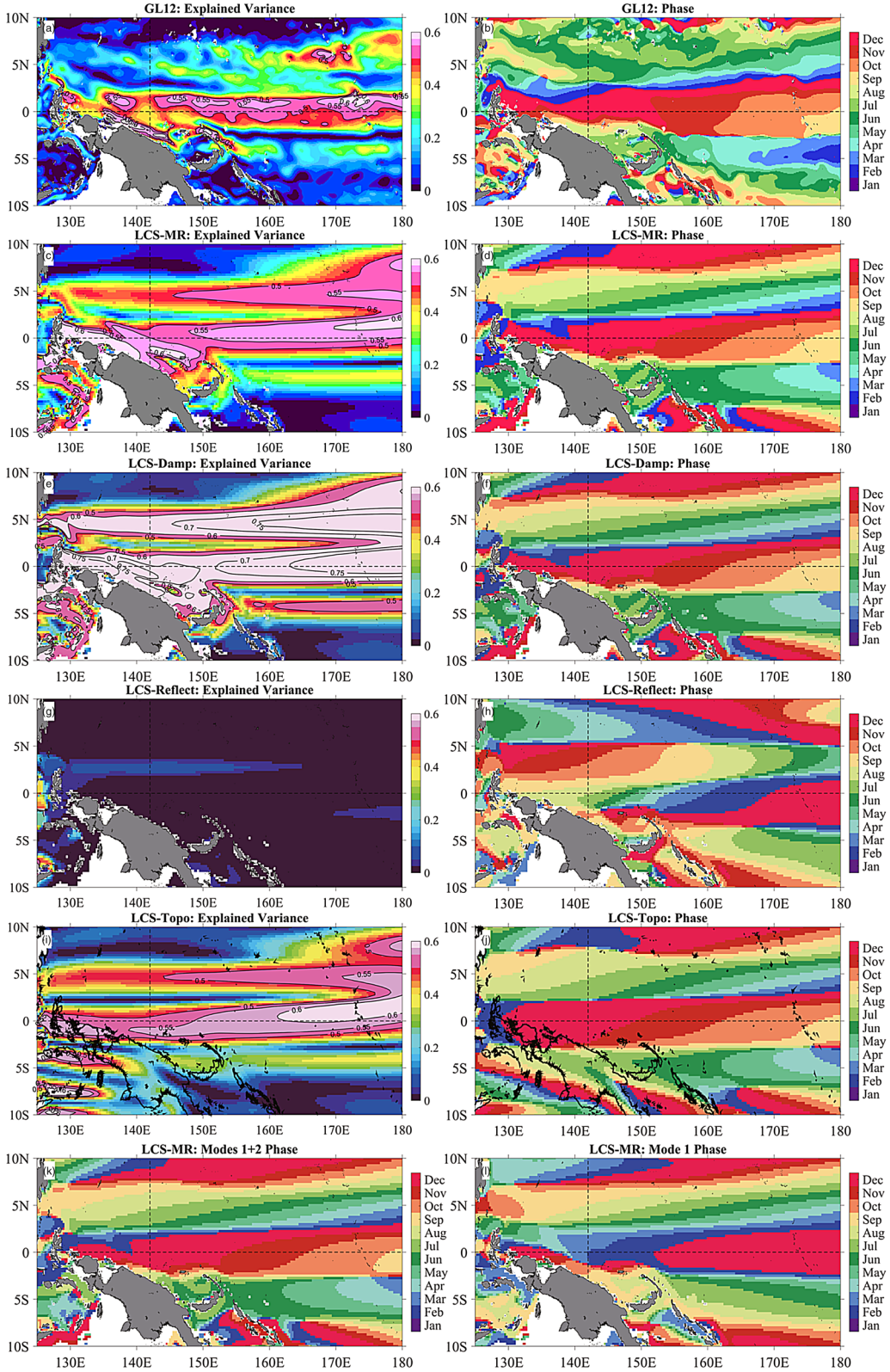

Figure 3. The annual harmonic of monthly intermediate zonal velocities in the western Pacific: explained variance and phase from (a, b) GL12, (c, d) LCS-MR, (e, f) LCS-Damp, (g, h) LCS-Reflect, and (i, j) LCS-Topo, and phase from LCS-MR baroclinic (k) modes 1 + 2 and (l) mode 1. Two reference dashed lines denote the equator and 142°E. LCS, linear continuously stratified ocean model.

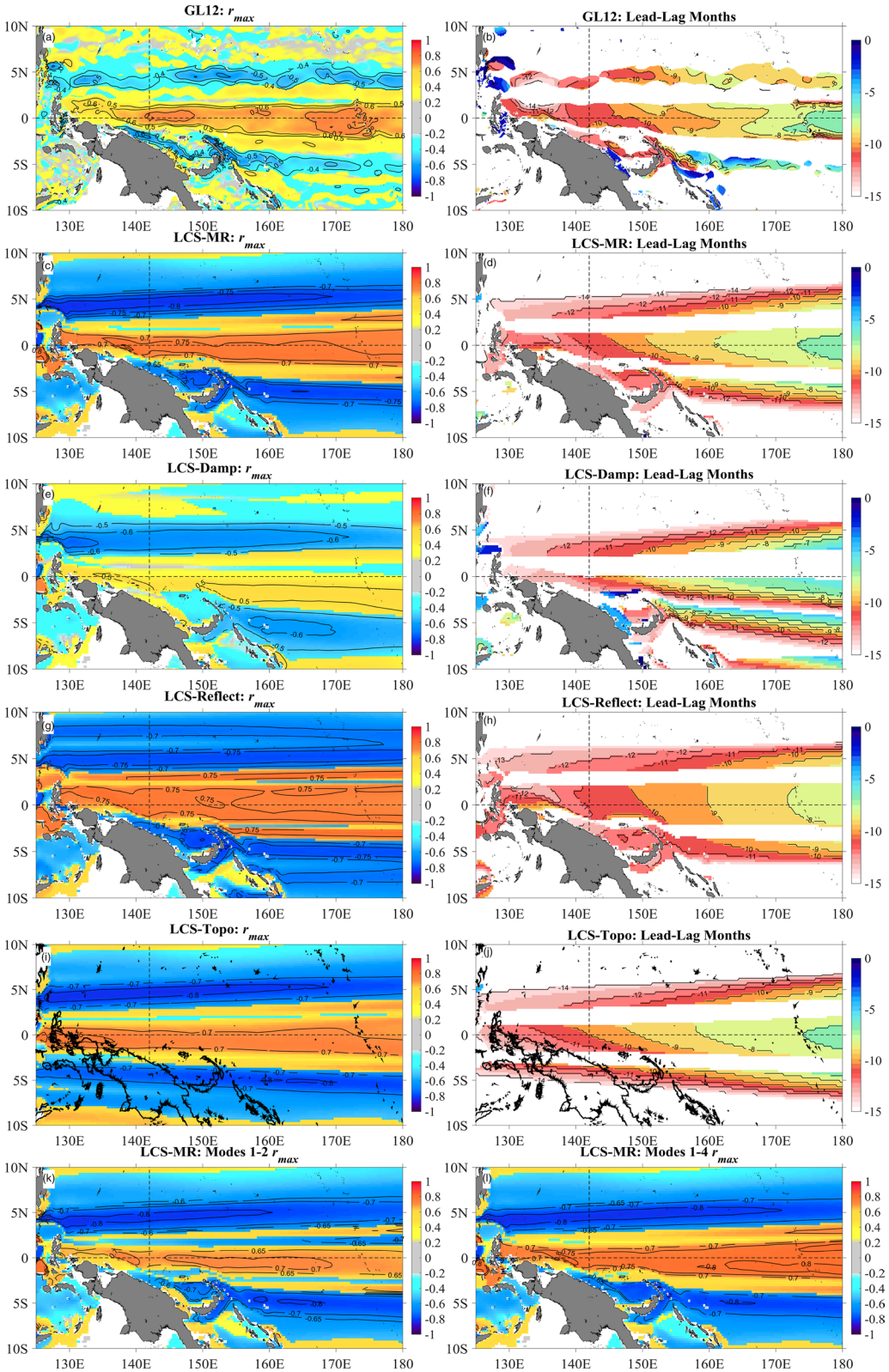
GL12: r_{max}
GL12: Lead-Lag Months
LCS-MR: r_{max}
LCS-MR: Lead-Lag Months
LCS-Damp: r_{max}
LCS-Damp: Lead-Lag Months
LCS-Reflect: r_{max}
LCS-Reflect: Lead-Lag Months
LCS-Topo: r_{max}
LCS-Topo: Lead-Lag Months
LCS-MR: Modes 1-2 r_{max}
LCS-MR: Modes 1-4 r_{max}
10N
5N
0
5S
10S
130E
140E
150E
160E
170E
180

an anticlockwise connected circulation for the La Niña events (Figures S1b and S1c). An El Niño (La Niña) event is defined as a period when the 3-month running mean of Niño-3.4 exceeds 0.5°C (falls below −0.5°C) for at least five consecutive months following the NOAA definition.

The above findings can be further revealed by the horizontal distribution of GL12 r_{max} (Figure 4a). The four regions with absolute $r_{max} > 0.40$ include the southern zonal band along ~5°S over 155°E−175°E, the western boundary NGCUC-I region over 138°E−155°E, the LEIC zonal band straddling the equator over 130°E−180°, and the northern zonal band along ~5°N over 130°E−180°. Their corresponding time lagging behind the Niño-3.4 index is 7–12 months, increasing from east to west (Figure 4b). LCS-MR faithfully reproduces the lead-lag correlations of the GL12 LEIC and NGCUC-I transport anomalies at 142°E with the Niño-3.4 index (Figures 2g and 2h), and the distributions of GL12 r_{max} and the lead-lag months (Figures 4c and 4d), especially for the LEIC and NGCUC-I regions. This suggests that LCS-MR can be used to study the mechanism responsible for the interannual variability in intermediate currents.

To investigate the contribution of different baroclinic modes, we examine their corresponding distributions of r_{max}. The first baroclinic mode plays a minor role in the interannual variability because absolute r_{max} is generally less than 0.60 (horizontal distribution is not shown, and the result along 142°E is shown in Figure S4a). When the second baroclinic mode is added, the four regions of the northern and southern zonal bands, the LEIC, and the NGCUC-I with absolute $r_{max} > 0.60$ appear, but the magnitudes of the absolute r_{max} in the LEIC and NGCUC-I bands are low (Figure 4k). Including the third baroclinic mode does not change the pattern much (Figure S4a), suggesting the insignificant role of this mode. When baroclinic mode 4 is incorporated, the peak values of the positive r_{max} in the LEIC band and negative r_{max} in the NGCUC-I band intensify, and those in the northern and southern bands almost stay the same (Figure 4l vs. Figure 4k). The distribution of lead-lag months for the sum of modes 1–4 greatly resembles that of the total 10 modes (figure not shown). The further inclusion of baroclinic mode 5 only leads to a small increase in the positive r_{max} in the LEIC region (Figure S4a). The above analyses demonstrate that the interannual variability in the LEIC and NGCUC-I is mainly induced by baroclinic modes 2 and 4, while that of the northern and southern zonal bands is mainly caused by baroclinic mode 2.

The relative importance of Rossby waves from the direct wind forcing and the reflection of Kelvin waves to the intermediate interannual variability is evaluated based on the analyses of the LCS-Damp (Figures 4e and 4f) and LCS-Reflect outputs (Figures 4g and 4h). In the northern and southern bands, the r_{max} value of –0.7 to –0.8 in LCS-MR decreases to −0.6 in LCS-Damp and to –0.7 to –0.75 in LCS-Reflect. In the LEIC region, the r_{max} value of 0.7–0.75 in LCS-MR is reduced to 0.4–0.5 in LCS-Damp and is slightly enhanced to 0.75 in LCS-Reflect. Their corresponding lagged months decrease and increase in LCS-Damp and LCS-Reflect, respectively. In the NGCUC-I region, LCS-Damp fails to simulate its response to ENSO with the opposite sign of r_{max}. Instead, LCS-Reflect successfully reproduces such a response. For the LEIC and NGCUC-I transports at 142°E, their anomalies obtained from LCS-Reflect (almost the same as their original time series due to the small seasonal amplitude) positively and negatively follow the Niño-3.4 index very well at a lag of 10–11 months, respectively (Figure 2e). The values of r_{max} from LCS-Reflect are close to those from LCS-MR and are much larger than those from LCS-Damp (Figures 2g and 2h). For r_{max} of baroclinic modes 1 + 2 at 142°E, LCS-Reflect shows a similar latitudinal distribution but with a much larger absolute value, and LCS-Damp shows an opposite sign in the LEIC and NGCUC-I regions compared to LCS-MR (Figures S4b and S4c vs. Figure S4a). This suggests the negative effect of direct wind-forced Rossby wave. LCS-Reflect r_{max} stays the same when baroclinic modes higher than 2 are added. Thus, when baroclinic mode 4 is added, the slight increase in the LCS-MR absolute r_{max} in the LEIC and NGCUC-I regions is attributed to the direct wind-forced Rossby wave. Therefore, the reflected Kelvin-to-Rossby wave plays a decisive role in the interannual response of intermediate currents to ENSO. The direct wind-forced Rossby wave mostly weakens this interannual response, although in a small part it has a positive effect.

Figure 4. The lead-lag correlation between intermediate zonal velocity anomalies and the Niño-3.4 index in the western Pacific: the peak values of correlation coefficients (r_{max}) and the corresponding lead-lag months from (a, b) GL12, (c, d) LCS-MR, (e, f) LCS-Damp, (g, h) LCS-Reflect, and (i, j) LCS-Topo, and the value of r_{max} from LCS-MR baroclinic modes (k) 1–2 and (l) 1–4. For lead-lag months, color shading depicts regions with absolute $r_{max} > 0.40$ in GL12 and LCS-Damp and absolute $r_{max} > 0.60$ in LCS other experiments. Two reference dashed lines denote the equator and 142°E. LCS, linear continuously stratified ocean model.

To examine the influence of the PNG coastline on the interannual variability, we discuss the changes in the r_{max} and lead-lag-month distributions between LCS-MR (Figures 4c and 4d) and LCS-Topo (Figures 4i and 4j). Compared to LCS-Topo, the LEIC region with $r_{max} > 0.7$ expands in the meridional range, and its r_{max} value intensifies in LCS-MR. The southern band with negative $r_{max} < -0.6$ is shifted northward along the PNG coastline, and the intensity of negative r_{max} over 138°E–145°E weakens from −0.7 in LCS-Topo to −0.65 in LCS-MR. The northern band with negative $r_{max} < -0.6$ remains the same. For the distribution of lead-lag months, the time lagging behind the Niño-3.4 index in the LEIC band over 140°E–150°E increases by 1 month from LCS-Topo to LCS-MR.

4. Conclusions

The LEIC and NGCUC-I exhibit strong seasonal variations and a significant interannual response to ENSO at a 7–12-month lag. The seasonal variability is mainly induced by the first meridional and the sum of the first two baroclinic Rossby waves. The contribution from the second baroclinic mode is essential for the phase of the seasonal cycle, but it reduces the magnitude of the seasonal explained variance. The interannual variability in the LEIC and NGCUC-I is induced by baroclinic modes 2 and 4 Rossby waves. The Rossby wave from direct wind forcing plays a decisive role in the seasonal variability of intermediate currents, while that from the reflection of Kelvin waves exerts a crucial influence on intermediate interannual variability. The existence of the PNG coastline enhances the seasonal variance in the LEIC region west of 145°E and the phase difference between the LEIC and NGCUC-I regions and intensifies the interannual relationship between the LEIC and ENSO.

Data Availability Statement

The mooring data analyzed in this paper are available for download at https://doi.org/10.5281/zenodo.4422130. CCMP v2.0 wind field data are produced by Remote Sensing Systems (http://www.remss.com/measurements/ccmp). The GL12 product is available on the Copernicus Marine Environment Monitoring Service website (https://resources.marine.copernicus.eu/?option=com_csw&view=details&product_id=GLOBAL_REANALYSIS_PHY_001_030). The Niño-3.4 index is downloaded from https://psl.noaa.gov/gcos_wgsp/Timeseries/Data/nino34.long.anom.data.

Acknowledgments
We are sincerely grateful to all the researchers, staff, and the crew of R/V Kexue (Science) for their efforts in conducting the mooring measurements during 2014–2018. Comments from William Kessler and the other anonymous reviewer help to improve the manuscript substantially. We thank the TOCS Project for providing two mooring data at 142°E/2.5°S and 138°E/0° (http://www.jamstec.go.jp/ipobs/adcp/adcp_data.html). This study is supported by the National Natural Science Foundation of China (grants 91958204 and 41776022), the Strategic Priority Research Program of the Chinese Academy of Sciences (grant XDA22000000), and the Key Research Program of Frontier Sciences, CAS (grant QYZDB-SSW-SYS034). F. Wang thanks the support from the National Natural Science Foundation of China (grants 41730534 and 41421005). Q. Ma thanks the support by the National Natural Science Foundation of China (grants 42006003) and the China Ocean Mineral Resources Research and Development Association Program (DY135-E2-3-02). D. Zhang is supported by the Joint Institute for the Study of the Atmosphere and Ocean (JISAO) under NOAA Cooperative Agreement NA15OAR4320063.

References

Ascani, F., Firing, E., Dutrieux, P., McCreary, J. P., & Ishida, A. (2010). Deep equatorial ocean circulation induced by a forced-dissipated Yanai beam. *Journal of Physical Oceanography*, *40*(5), 1118–1142.

Ascani, F., Firing, E., McCreary, J. P., Brandt, P., & Greatbatch, R. J. (2015). The deep equatorial ocean circulation in wind-forced numerical solutions. *Journal of Physical Oceanography*, *45*(6), 1709–1734.

Atlas, R., Hoffman, R. N., Ardizzone, J., Leidner, S. M., Jusem, J. C., Smith, D. K., & Gombos, D. (2011). A cross-calibrated, multiplatform ocean surface wind velocity product for meteorological and oceanographic applications. *Bulletin of the American Meteorological Society*, *92*(2), 157–174. https://doi.org/10.1175/2010BAMS2946.1

Cravatte, S., Kessler, W. S., & Marin, F. (2012). Intermediate zonal jets in the tropical Pacific Ocean observed by Argo floats. *Journal of Physical Oceanography*, *42*(9), 1475–1485.

Cravatte, S., Kestenare, E., Marin, F., Dutrieux, P., & Firing, E. (2017). Subthermocline and intermediate zonal currents in the tropical Pacific Ocean: Paths and vertical structure. *Journal of Physical Oceanography*, *47*(9), 2305–2324.

d'Orgeville, M., Hua, B. L., & Sasaki, H. (2007). Equatorial deep jets triggered by a large vertical scale variability within the western boundary layer. *Journal of Marine Research*, *65*(1), 1–25.

Eriksen, C. C. (1981). Deep currents and their interpretation as equatorial waves in the western Pacific Ocean. *Journal of Physical Oceanography*, *11*(1), 48–70.

Firing, E. (1987). Deep zonal currents in the central equatorial Pacific. *Journal of Marine Research*, *45*(4), 791–812.

Firing, E., Wijffels, S. E., & Hacker, P. (1998). Equatorial subthermocline currents across the Pacific. *Journal of Geophysical Research*, *103*(C10), 21413–21423.

Gouriou, Y., Delcroix, T., & Eldin, G. (2006). Upper and intermediate circulation in the western equatorial Pacific Ocean in October 1999 and April 2000. *Geophysical Research Letters*, *33*, L10603. https://doi.org/10.1029/2006GL025941

Gouriou, Y., & Toole, J. (1993). Mean circulation of the upper layers of the western equatorial Pacific Ocean. *Journal of Geophysical Research*, *98*(C12), 22495–22520.

Hua, B. L., d'Orgeville, M., Fruman, M. D., Ménesguen, C., Schopp, R., Klein, P., & Sasaki, H. (2008). Destabilization of mixed Rossby gravity waves and the formation of equatorial zonal jets. *Journal of Fluid Mechanics*, *610*, 311–341.

Ishizaki, H., Nakano, H., Nakano, T., & Shikama, N. (2014). Evidence of equatorial Rossby wave propagation obtained by deep mooring observations in the western Pacific Ocean. *Journal of Oceanography*, *70*(6), 463–488.

Johnson, G. C., Sloyan, B. M., Kessler, W. S., & McTaggart, K. E. (2002). Direct measurements of upper ocean currents and water properties across the tropical Pacific during the 1990s. *Progress in Oceanography*, *52*(1), 31–61. https://doi.org/10.1016/S0079-6611(02)00021-6

Kawabe, M., Kashino, Y., & Kuroda, Y. (2008). Variability and linkages of New Guinea coastal undercurrent and lower equatorial intermediate current. *Journal of Physical Oceanography*, *38*(8), 1780–1793. https://doi.org/10.1175/2008JPO3916.1

Kessler, W. S., & McCreary, J. P. (1993). The annual wind-driven Rossby wave in the subthermocline equatorial Pacific. *Journal of Physical Oceanography*, *23*(6), 1192–1207.

Kuroda, Y. (2000). Variability of currents off the northern coast of New Guinea. *Journal of Oceanography*, *56*, 103–116.

Lellouche, J.-M., Greiner, E., Le Galloudec, O., Garric, G., Regnier, C., Drevillon, M., et al. (2018). Recent updates to the Copernicus Marine Service global ocean monitoring and forecasting real-time 1⁄12° high-resolution system. *Ocean Science*, *14*(5), 1093–1126. https://doi.org/10.5194/os-14-1093-2018

Ma, Q., Wang, J., Wang, F., Zhang, D., Zhang, Z., & Lyu, Y. (2020). Interannual variability of lower equatorial intermediate current response to ENSO in the Western Pacific. *Geophysical Research Letters*, *47*, e2020GL089311. https://doi.org/10.1029/2020GL089311

Marin, F., Kestenare, E., Delcroix, T., Durand, F., Cravatte, S., Eldin, G., et al. (2010). Annual reversal of the Equatorial Intermediate Current in the Pacific: Observations and model diagnostics. *Journal of Physical Oceanography*, *40*(5), 915–933. https://doi.org/10.1175/2009JPO4318.1

McCreary, J. P. (1981). A linear stratified ocean model of the coastal undercurrent. *Philosophical Transactions of the Royal Society of London, Series A*, *302*, 385–413.

Ménesguen, C., Delpech, A., Marin, F., Cravatte, S., Schopp, R., & Morel, Y. (2019). Observations and mechanisms for the formation of deep equatorial and tropical circulation. *Earth and Space Science*, *6*, 370–386. https://doi.org/10.1029/2018EA000438

Qiu, B., Chen, S., & Sasaki, H. (2013). Generation of the north equatorial undercurrent jets by triad baroclinic Rossby wave interactions. *Journal of Physical Oceanography*, *43*(12), 2682–2698.

Shankar, D., McCreary, J. P., Han, W., & Shetye, S. R. (1996). Dynamics of the East India Coastal Current: 1. Analytic solutions forced by interior Ekman pumping and local alongshore winds. *Journal of Geophysical Research*, *101*(C6), 13975–13991.

Ueki, I., Kashino, Y., & Kuroda, Y. (2003). Observation of current variations off the New Guinea coast including the 1997–1998 El Niño period and their relationship with Sverdrup transport. *Journal of Geophysical Research*, *108*(C7), 3243. https://doi.org/10.1029/2002JC001611

Wang, F., Li, Y., & Wang, J. (2016). Intraseasonal variability of the surface zonal currents in the western tropical Pacific Ocean: Characteristics and mechanisms. *Journal of Physical Oceanography*, *46*(12), 3639–3660. https://doi.org/10.1175/JPO-D-16-0033.1

Wang, Q., Wang, F., Feng, J., Hu, S., Zhang, L., Jia, F., & Hu, D. (2019). The Equatorial Undercurrent and its origin in the region between Mindanao and New Guinea. *Journal of Geophysical Research: Oceans*, *124*, 2313–2330. https://doi.org/10.1029/2018JC014842

Yu, X., & McPhaden, M. J. (1999). Seasonal variability in the equatorial Pacific. *Journal of Physical Oceanography*, *29*(5), 925–947.

Zenk, W., Siedler, G., Ishida, A., Holfort, J., Kashino, Y., Kuroda, Y., et al. (2005). Pathways and variability of the Antarctic Intermediate Water in the western equatorial Pacific Ocean. *Progress in Oceanography*, *67*, 245–281.

Zhang, Z., Pratt, L. J., Wang, F., Wang, J., & Tan, S. (2020). Intermediate intraseasonal variability in the western tropical Pacific Ocean: Meridional distribution of equatorial Rossby waves influenced by a tilted boundary. *Journal of Physical Oceanography*, *50*, 921–933.